Hotspots of Monthly Land Precipitation Variations Affected by SST Anomalies

Xiaofan Li,[a,b] Zeng-Zhen Hu,[c] Zhiqiang Gong,[d,e] and Bhaskar Jha[c,f]

[a] *Key Laboratory of Geoscience Big Data and Deep Resource of Zhejiang Province, School of Earth Sciences, Zhejiang University, Hangzhou, Zhejiang, China*
[b] *Southern Marine Science and Engineering Guangdong Laboratory (Zhuhai), Zhuhai, China*
[c] *Climate Prediction Center, NCEP/NWS/NOAA, College Park, Maryland*
[d] *College of Physics and Electronic Engineering, Changshu Institute of Technology, Changshu, China*
[e] *Laboratory for Climate Studies, National Climate Research Center, China Meteorological Administration, Beijing, China*
[f] *ERT, Laurel, Maryland*

ABSTRACT: Climate predictability at seasonal to interannual time scales is mainly associated with sea surface temperature anomalies (SSTAs). How to quantitatively assess the impact of SSTAs on climate variability and predictability is an unresolved topic. Using a novel metric [bulk connectivity (BC)], the integrated influences of global SSTAs on precipitation anomalies over land are examined in observations and compared with Atmospheric Model Intercomparison Project (AMIP) simulations in 1957–2018. The hotspots of the land precipitation variation affected by global SSTA are identified, and the seasonality is evaluated. Such hotspots indicate the regions of land precipitation predictability caused by SSTAs. The hotspots are observed in the Sahel region in September–March, in the Indochina Peninsula in April and May, and in southwestern United States in December–March, which are mostly linked to the influence of El Niño–Southern Oscillation (ENSO). The overall impact of SSTAs on land precipitation is larger in the Southern Hemisphere than in the Northern Hemisphere. The spatial variations of BC and hotspots in the observations are partially reproduced in the AMIP simulations. However, an individual run in the AMIP simulations underestimates the integrated influence of global SSTA on land precipitation anomalies, while the ensemble mean amplifies the integrated influence, and both show a challenge in capturing the seasonality of the SST influence, particularly the time of the strongest impact. The results of the BC metric can serve as a benchmark to evaluate climate models and to identify the predictability sources.

KEYWORDS: Atmosphere-ocean interaction; ENSO; Precipitation; Climate models; Climate variability

1. Introduction

Climate anomalies and associated environmental hazards may cause serious social and economic crises, especially for some extreme events, such as severe droughts, floods, heatwaves, and wildfires. Due to the expansion of human activity and the growth of economics, the damage of these disasters may increase over time. For instance, in the United States, the number of weather- and climate-related disasters exceeding one billion dollars has increased since 1980. From 1980 to 2020, the average number of billion-dollar events was 7.1 per year, whereas it increased to 16.2 per year for 2016–20, including the consumer price index adjustments (https://www.globalchange.gov/browse/indicators/billion-dollar-disasters). Thus, understanding and predicting climate variability have been of vital importance both for economic growth and the safety of society.

From the predictability perspective, climate anomalies at seasonal to interannual time scales consist of unpredictable and predictable components (e.g., Kumar et al. 2001; Scaife and Smith 2018). The unpredictable component is mostly driven by the atmospheric internal dynamics, which mainly relies on initial conditions in a dynamical prediction system. Thus, it is largely unable to be predicted beyond 2–3 weeks and is referred to as "weather noise" in climate prediction of seasonal to interannual time scales. The predictable component at seasonal to interannual time scales is mainly forced by boundary forcing, particularly sea surface temperature (SST) (National Research Council 2010; He et al. 2016; Liang et al. 2019; Hu et al. 2020). That is the major basis for climate prediction operation at seasonal to interannual time scales in various climate centers (O'Lenic et al. 2008; Peng et al. 2012, 2013).

The mechanisms of the predictable component of climate variability vary by region. In the tropics, it is mainly and directly affected by zonally overturning atmospheric circulation linked to the atmosphere and ocean coupling, such as the Walker circulation associated with El Niño–Southern Oscillation (ENSO). For example, precipitation anomalies in northeastern Brazil are modulated by a shift of the Walker circulation (e.g., Kayano et al. 1988). Similarly, a longitudinal displacement and strength variation of the Walker circulation associated with ENSO modulate Indian summer monsoon variability (e.g., Ju and Slingo 1995). ENSO affects southern African rainfall variability by suppressing or enhancing the tropical convection over the subcontinent (e.g., Mason 2001).

The impact of SST anomalies (SSTAs) on the extratropical climate variability is more complicated and indirectly compared with the impact on the tropics. It is mainly through various teleconnections associated with tropical forcing (Bjerknes 1969; Wallace and Gutzler 1981; Ting and Sardeshmukh 1993; Yulaeva and Wallace 1994; Alexander et al. 2009; Stan et al.

2017; Yeh et al. 2018). For example, by generating a Pacific–North American (PNA)-like teleconnection pattern that alters the meridional location of the midlatitude jet stream, ENSO affects North American climate anomalies (Leathers et al. 1991; Li et al. 2019). In East Asia, the impact of ENSO is ultimately through altering the subtropical high in the western North Pacific. The Rossby-wave response to the diabatic heating associated with ENSO (e.g., Wang et al. 2000; Wu et al. 2003), the Pacific–Japan (PJ) pattern forced by the convective activities in the western tropical Pacific (e.g., Nitta 1987; Nitta and Hu 1996), and the Indo-western Pacific Ocean capacitor effect (Xie et al. 2016) are three of the potential mechanisms for the impact of ENSO on East Asian climate variability.

These teleconnections are the major contributors to the inherent climate predictability. It is expected that the prediction skill of extratropical climate variability in a climate model is linked to the ability of the model to reproduce the various teleconnections forced by SSTA. Nevertheless, it is a partially unresolved topic on how to quantitatively measure the ability of a model to reproduce the teleconnections. Through verifying the ability of a model to reproduce the integrated connections, we can identify the model's defects and find potential ways to improve the model and enhance its prediction skill. Although monthly mean precipitation over land is one of the most important climate variables of societal relevance, its prediction skill is quite low in operation (Peng et al. 2012, 2013). Thus, it is meaningful to choose monthly mean precipitation as the variable to examine its connection with SSTAs at seasonal to interannual time scales in observations and to identify the hotspots of land precipitation variability that are affected by SSTAs. Moreover, through comparing with the observations, the model's ability to capture the integrated connections is verified.

Recently, Hu et al. (2020) proposed a new metric to measure the bulk connectivity (BC) between two variables. With the BC metric, they identified the key regions of SSTA in forcing global land precipitation variability in all months as a whole in observations. Later, Li et al. (2022) used the metric to further identify the regions of SSTA having the most significant connections with global land precipitation anomaly and the seasonality. They confirmed that SSTAs in the tropical central and eastern Pacific associated with ENSO have the strongest influence on the global land precipitation anomaly, while SSTAs in the tropical Indian and Atlantic Oceans play a secondary role. Seasonally, the impact is the strongest in October and the weakest in June. Compared with the observational results, in addition to the biases in capturing the seasonality of the impact, a set of Atmospheric Model Intercomparison Project (AMIP) simulations amplified the strength of the impact in the ensemble mean, and underestimated it in an individual member of the AMIP simulations.

As a complement and extension of Hu et al. (2020) and Li et al. (2022), instead of identifying the key SST regions affecting global land precipitation variability in observations and AMIP simulations and the seasonality, in this work, using similar data and approaches, we examine the integrated influence of global SSTA as a whole on the variability of land precipitation at seasonal to interannual time scales and identify the hotspots of the land precipitation significantly affected by global SSTA as well as the seasonality. Such hotspots of land precipitation imply predictability regions due to the SST influence through various teleconnections. That provides a physical basis for climate prediction. Moreover, through comparison with AMIP simulations, we illustrate the fidelity and defects of a climate model in reproducing the land precipitation variability and the seasonality caused by SST forcing. Thus, although similar data and approaches are adopted, the objectives are different between this work and Li et al. (2022). Specifically, in this work, we focus on the following questions: 1) In which regions of land precipitation anomalies have significant connections with global SSTA as a whole? In other words, where are the hotspots of land precipitations that are significantly affected by SSTA in observations? 2) What are the latitudinal variation and seasonal evolution of the connection? 3) How well can the AMIP simulation capture the observed spatial variations of the connection and the seasonality from an individual member and ensemble mean perspective?

Such assessment in the present work can set up a benchmark validating a climate model in capturing the bulk connection between SSTA and land precipitation variation and identifying the predictability sources of regional precipitation over land. Meanwhile, the differences between the observations and model simulations link to model defects and may imply a potential for model improvement in capturing the impact of SSTAs on land precipitation variability. The paper is organized as the follows. Section 2 introduces the data and methods used in this work; sections 3 and 4 show the results of the observations and AMIP simulations, respectively. Section 5 displays the hemispheric averages and seasonality. Section 6 summarizes the results with some discussion.

2. Data and methods

The observation-based monthly mean SSTs used in this work are the Met Office Hadley Centre's sea ice and SST version 2 (HadISSTv2) with a $1° \times 1°$ resolution (Rayner et al. 2006). The SST dataset is an analysis combining in situ sea surface observations and satellite-derived estimates with bias correlations of the bucket observations. The monthly mean reconstructed precipitation analysis from January 1948 to December 2018 on a $1° \times 1°$ spatial resolution (PRECP; Chen et al. 2002) is examined. PRECP was developed by the optimal interpolation of gauge observations over land only. As a robustness check, the monthly mean precipitation analysis over land from version 4.03 of the monthly high-resolution gridded dataset of the Climatic Research Unit (CRU) with a $0.5° \times 0.5°$ resolution is also examined. The CRU data are derived from the interpolation of monthly anomalies from extensive networks of weather station observations by using angular-distance weighting (Harris et al. 2020). The precipitation data are interpolated into a $1° \times 1°$ resolution in the calculations.

To assess the response of land precipitation to SST, the AMIP simulations are analyzed. The AMIP simulations are from the Global Forecast System (GFS), which is forced by
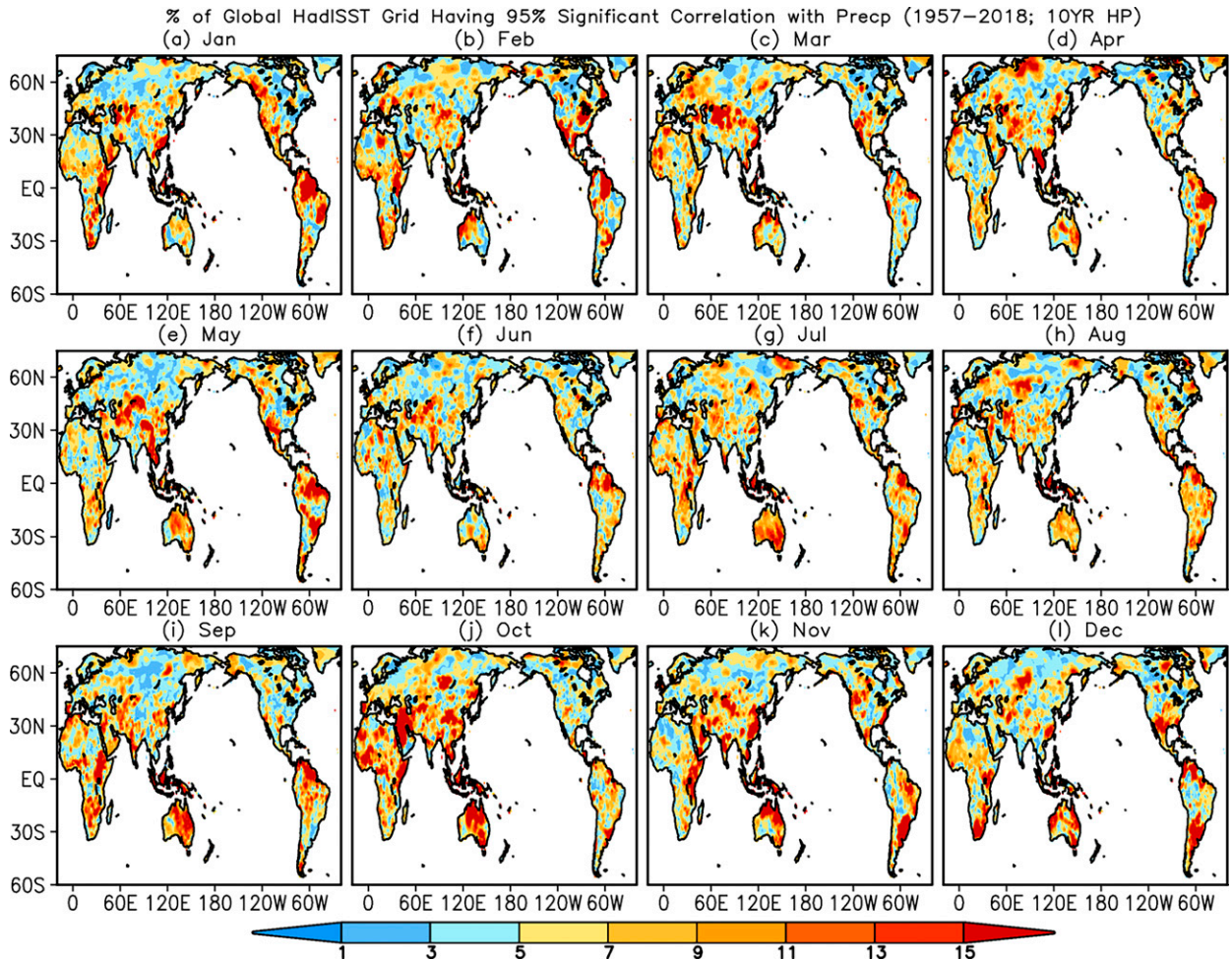
FIG. 1. Bulk connectivity (BC) in the observations. BC is defined as the percentage of accumulated latitudinal-weighted grid numbers for the correlation between land precipitation anomaly at a grid and global SSTA in each month that reaches a 95% significance level using a t test, referred to latitudinal-weighted total grid number of global SSTA during January 1957–December 2018. The significance areas are displayed in warm color with values equal to or larger than 5.

observed time-varying global monthly mean SSTs and sea ice from HadISST datasets for 1957–2008 (Rayner et al. 2006) and the Optimum Interpolation SST version 2 (OISSTv2) afterward (Reynolds et al. 2002). The simulations consist of 17 ensemble members with slightly different atmospheric initial conditions and cover the period from January 1957 to December 2018 (Hu et al. 2020; Li et al. 2022). The GFS is the atmospheric component of version 2 of the Climate Forecast System (CFSv2; Saha et al. 2014) with a horizontal resolution of T126 (~105 km) and 64 vertical levels.

In this work, the common period (January 1957–December 2018) of the observation-based data and the AMIP simulations is analyzed. The anomalies are referred to the monthly climatology in January 1981–December 2010. To eliminate the influence of decadal and longer-time variations, as well as the long-term trend, a 10-yr high-pass filter and detrending are applied to the data before the following calculations.

Similar to Hu et al. (2020); see their Fig. 5) and Li et al. (2022), the integrated connection of SSTA with precipitation

variability is measured by bulk connectivity (BC), a quantitative measure of the integrated connection of precipitation anomaly at a land grid point (L_i, L_j) with SSTA at a global oceanic grid point (Om, On):

$$\mathrm{BC}_{(L_i, L_j)} = \frac{100}{N \times M_w} \sum_{\mathrm{Om}=1}^{M} \sum_{\mathrm{On}=1}^{N} \delta^{\alpha}_{(L_i,L_j;\mathrm{Om,On})}. \quad (1)$$

In Eq. (1), $\delta^{\alpha}_{(L_i,L_j;\mathrm{Om,On})} = 1$ if the correlation of precipitation anomaly at grid (L_i, L_j) with SSTA at grid (Om, On) exceeds the statistical significance level α (here, we chose 95%), and $\delta^{\alpha}_{(L_i,L_j;\mathrm{Om,On})} = 0$ if the correlation is not significant. Here M and N are the zonal and meridional grid numbers of global SSTA from 90°S to 90°N in this work, respectively. The term $M_w = \sum_{\mathrm{On}=1}^{N} W(\mathrm{On})$ is the latitudinal (area) weighted total meridional grid number of SST. Thus, BC is defined as the percentage of accumulated latitudinal weighted grid numbers for the correlation between land precipitation anomaly at a grid and global SSTA in each month that reaches a 95%

Zonal Mean % of HadISST Grid Having 95% Significant Correlation with Land Precp
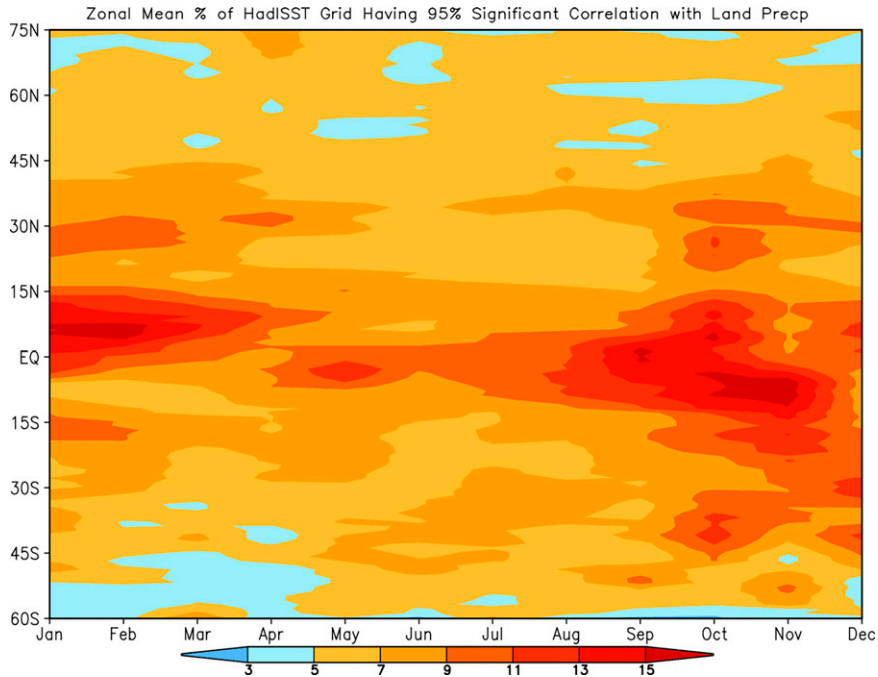
FIG. 2. As in Fig. 1, but for the zonal average.

significance level using a *t* test, referred to as the latitudinal-weighted total grid number of global SSTA. Similar to Li et al. (2022), through Monte Carlo simulations with SST replaced by random time series, it is suggested that, statistically, at the significance level of 95%, land grid points with $BC_{(L_i, L_j)} > 5$

denote that precipitation anomaly at the grid point may have a statistically significant connection with SSTA over some regions, while $BC_{(L_i, L_j)} < 5$ means no significant connection. This metric can be applied to any two variables in any region to quantitatively measure their statistical BC, and also to
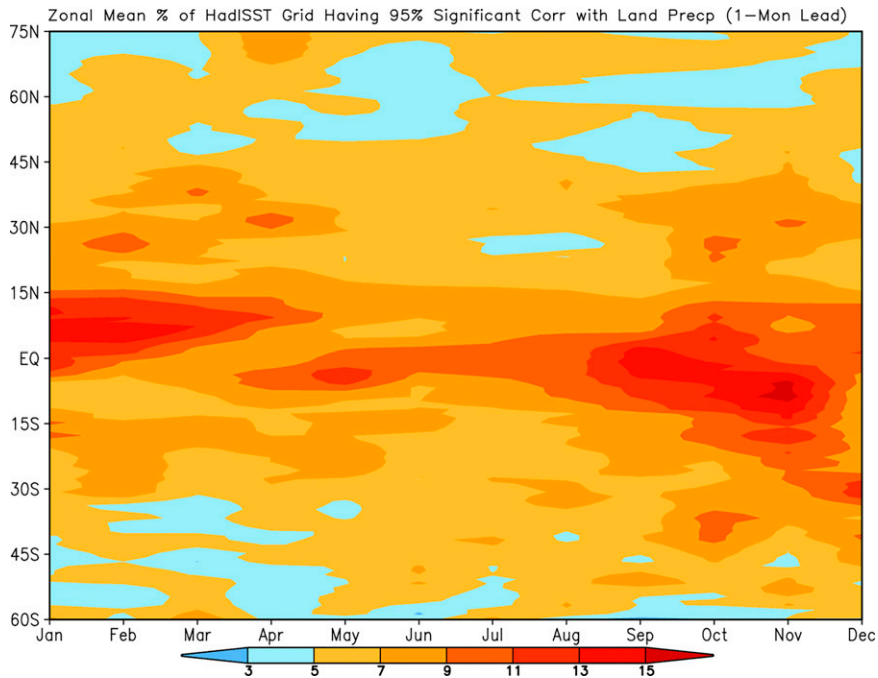
Zonal Mean % of HadISST Grid Having 95% Significant Corr with Land Precp (1−Mon Lead)

FIG. 3. As in Fig. 2, but for SST leading precipitation by 1 month.
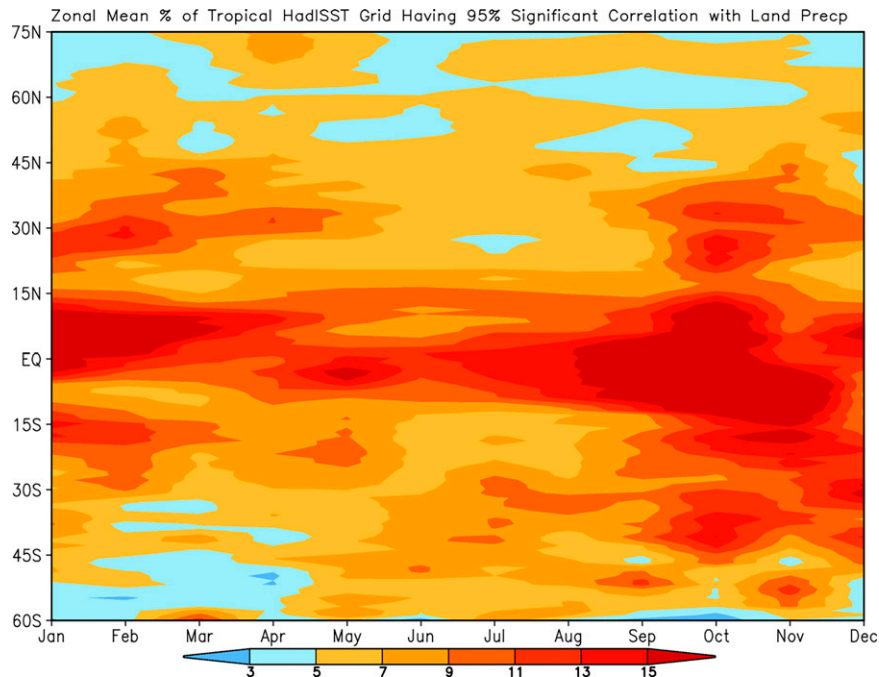
FIG. 4. As in Fig. 2, but for the SST in the tropics (30°S–30°N) only.

evaluate the ability of a climate model in capturing the observed connections of two variables.

3. Hotspots in the observations and connections with ENSO

Figure 1 shows the spatial distribution of monthly BC over the global land with warm colors representing the significance at the level of 95%. Overall, the values of BC are larger in the low latitudes than in the high latitudes, which is more evident in the zonal mean shown in Fig. 2, implying a decrease of the impact of SST anomaly on land precipitation variations from low to high latitudes. Geographically, there are some hotspots with large BC values, such as in the Sahel region, central Asia, the Indochina Peninsula, tropical South America, southwestern United States, subtropical Africa, and northern Australia. That means the precipitation anomalies over these regions may be significantly affected by SSTA and predictable to some extent.

In addition to the geographical variations, there is a distinguished month-to-month change of the BC distribution. In other words, the hotspots show up in some months and disappear in other months. For instance, the hotspot in the Sahel region emerges in September–March and disappears in April–August. In the Indochina Peninsula, the hotspot only presents in April and May. In southwestern United States, the hotspot is seen in December–March. The seasonal and latitudinal variations of the BC are more visible in the zonal mean shown in Fig. 2. Overall, in addition to the geographic dependence (Fig. 1), as shown in the zonal mean of BC (Fig. 2), the BC values have pronounced seasonality with larger values in the boreal winter and autumn and smaller values in boreal spring and summer in the Northern

Hemisphere. For the Southern Hemisphere, it is larger in austral spring and summer than in austral autumn and winter. It should be indicated that the results shown in Figs. 1 and 2 are similar if the CRU precipitation data are used in the calculations (not shown).

To check the lag impact of SST on precipitation (Wang and Fu 2000; Kumar and Hoerling 2003), we repeat the calculations with SST leading precipitation by 1 month. It is noted that both the spatial distribution of BC in each month (not shown) and the zonal average of the monthly and latitudinal variations (Fig. 3) are similar to the simultaneous ones (Figs. 1 and 2), but the overall amplitudes are slightly smaller in the former (Fig. 3) than in the latter (Figs. 1 and 2). It is suggested that the collective influence of the SSTA can reach land precipitation mainly within one month. In the following analyses, we focus on the simultaneous connectivity between SST and land precipitation anomalies.

It is expected that most of the hotspots and their seasonal variations shown in Figs. 1 and 2 may be linked to the influence of tropical SST, especially ENSO. To verify the importance of the tropical SST to the land precipitation variation, we repeat the BC calculations with SST confined in the tropics (30°S–30°N). The spatial and monthly variations of the BC (not shown) are similar to Fig. 1. Such similarity is evident in the corresponding zonal mean (Figs. 2 and 4). Among the tropical SSTA, the SSTAs in the central and eastern tropical Pacific associated with ENSO play the most important role. By comparing the month-to-month BC (Fig. 1) with the correlations of land precipitation with SSTA indices (such as the Niño-3.4 index; Fig. 5), we can further identify which hotspots may be mainly driven or not driven by ENSO. For example, the hotspots in tropical South America and central Asia in
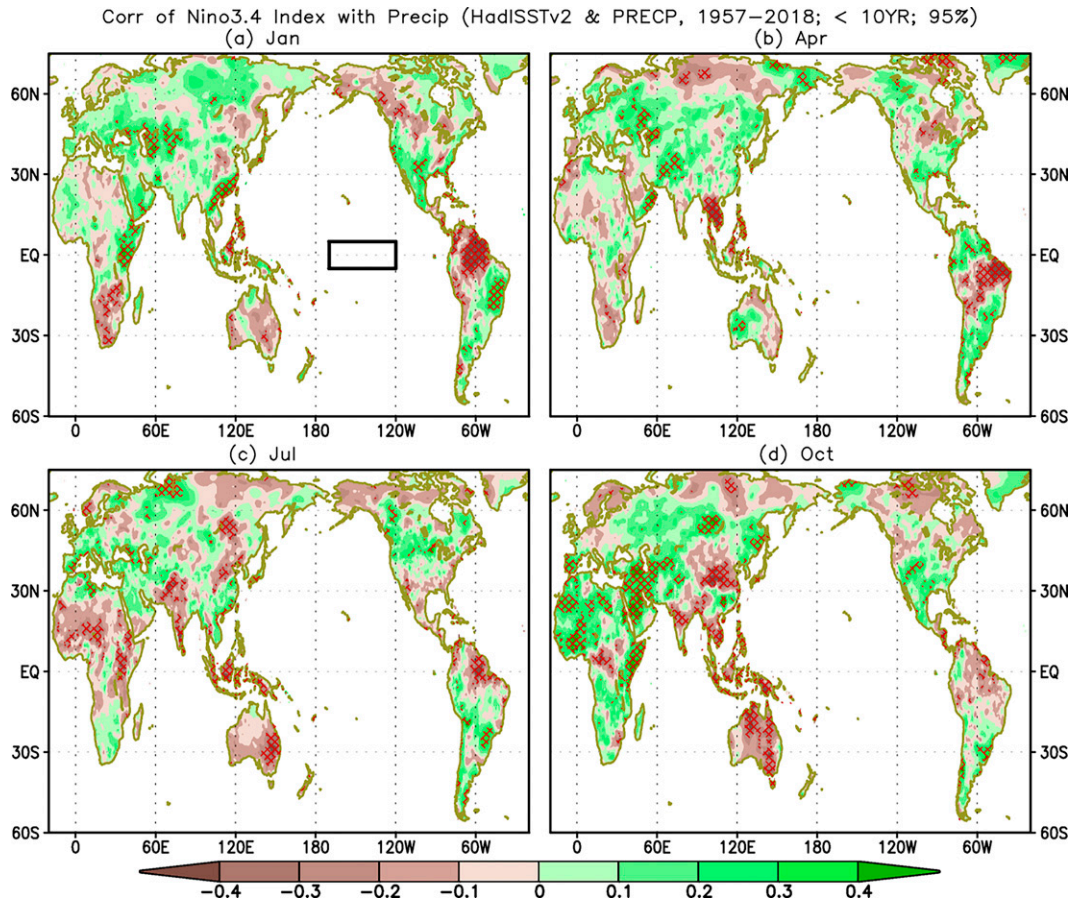
FIG. 5. Simultaneous correlations of observed land precipitation anomalies with the Niño-3.4 index in (a) January, (b) April, (c) July, and (d) October during 1957–2018. Hatching denotes significant correlations at the significance level of 95% using a *t* test.

January–April and the Indochina Peninsula in April and May (Fig. 1) seem due to the influence of ENSO (Fig. 5a). Meanwhile, we see that there are a lot of detailed differences between Figs. 1 and 5. For example, there are large BC values in Western Australia in July (Fig. 1g), but the correlations with ENSO are insignificant in the region (Fig. 5c), implying that the precipitation variation in Western Australia in July may not be driven by ENSO. That is a potential advantage of BC that aggregates the impacts of global SSTA, beyond just ENSO's impacts, on land precipitation. The comparison is more straightforward from the monthly and latitudinal variations of their zonal means (Figs. 2 and 6). The overall patterns are similar, implying that the monthly BC distributions are largely determined by the impact of ENSO. In particular, the large BC values between 0° and 15°N during January–April (Figs. 1 and 2) may be linked to the influence of ENSO on the precipitation anomalies in both the Horn of Africa and the Indochina Peninsula, and also in tropical South America in January and February (Figs. 5 and 6), while large BC values in the tropical land during July–December (Figs. 1 and 2) may reflect the collective impact of ENSO on the precipitation variations in tropical Africa, tropical Asia, the Maritime

Continent, and tropical South America (Figs. 5 and 6). That is generally consistent with some previous works, such as Ropelewski and Halpert (1987, 1996).

The impacts of SSTAs in different ocean basins on precipitation variations in different land areas may occur through different mechanisms (e.g., Alexander et al. 2002; Lau and Nath 2003). In addition to the direct impact of SSTAs in the tropical central and eastern Pacific associated with ENSO, SSTAs in the other ocean basins, such as the Indian and Atlantic Oceans, may also play an important role in land precipitation variation in some regions, which have been well documented (National Research Council 2010). For example, the large BCs in Western Australia in July (Fig. 1g) may be driven by Indian Ocean dipole mode, instead of ENSO (Ashok et al. 2003). Nevertheless, these SSTAs may be partially due to the interbasin lead–lag connections through atmospheric bridges or/and oceanic tunnels, and/or local atmosphere–ocean interactions (Wang et al. 2013; Cai et al. 2019; Wang 2019). In other words, considerable fractions of the SST variabilities in the tropical Indian and Atlantic Oceans are due to lag impacts of ENSO (Kug and Kang 2006; Hu et al. 2011; He et al. 2020; Zhang et al. 2021; and
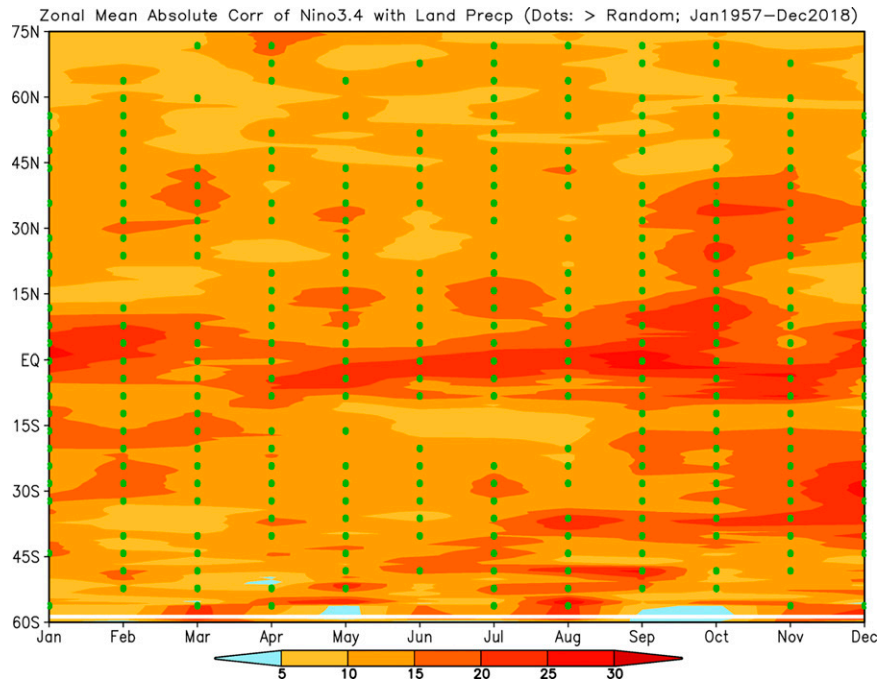
FIG. 6. Zonal mean of the *absolutely* simultaneous correlations of observed land precipitation anomalies with the Niño-3.4 index in each month during 1957–2018. Dots denote that the absolutely simultaneous correlations are larger than the corresponding absolutely simultaneous correlations of observed land precipitation anomalies with random numbers in each month.

references therein). For example, ENSO has its impact on East Asian summer precipitation through the delayed impact of SSTA over the tropical Indian Ocean. The ENSO-induced warm SSTA in the tropical Indian Ocean modulates the East Asian summer climate by stimulating an anomalous anticyclone over the western North Pacific in summer (Xie et al. 2009, 2016).

4. Hotspots in the AMIP simulations

a. Average of individual members

To further access the hotspots and their seasonal variations identified in the observations (Figs. 1 and 2), the corresponding results for the AMIP simulations are shown in Figs. 7 and 8. Through the comparisons between the observations and model simulations, the influence of SSTA on land precipitation variations can be further validated, which may also reflect the predictability of land precipitation variability. On the other hand, the dissimilarity might be due to sampling errors and/or defects in the AMIP simulations, meaning a potential for improvement. In a single member of the AMIP simulations, precipitation variability includes both the internal variability in the model and the response of the model to the observed SST specified in the AMIP integrations. To mimic the observations, the BC calculations with the AMIP simulations are done with each of the 17 individual members, and then their BC average is computed and shown in Figs. 7 and 8. Here, we call this the 17-member averaged BC.

Overall, the spatial distribution of the 17-member averaged BC of the AMIP simulations (Fig. 7) is similar to the corresponding observations (Fig. 1)—for instance, the hotspots in tropical South America in June–September, in central Asia in June–August, and in southwestern United States in February–March. However, the hotspots in the observations in the Sahel region, the Indochina Peninsula, and southwestern United States are vague in the AMIP simulations (Figs. 1 and 7). Also, BCs in central Asia in JJA are much weaker in the AMIP simulations than in the observations. Such differences are more noticeable in the zonal average (Figs. 2 and 8). The maximum values of BC present in the tropics during boreal summer in the AMIP simulations (Fig. 8), whereas they emerge in the tropics during July–December in the observations (Fig. 2). The relative maximum in the tropical Northern Hemisphere during January–April in the observations is qualitatively captured in the AMIP simulations (Figs. 2 and 8). It is reasonable to speculate that the unsuccessful reproductions of the connections between SST and extratropical land precipitation may be due to the defects in the model in capturing the land precipitation feature and the influence of SST-forced teleconnection. For example, in East Asian summer, the mean precipitation and its variability and connection with ENSO have pronounced differences in the AMIP simulations compared with the corresponding observations (see Fig. 11 of Liang et al. 2019).

Although there are many detailed differences, the BC latitudinal distributions with large values confined in the tropics (Figs. 2 and 8) are overall consistent with that of the signal-to-

% of Global SST Grid Having 95% Significant Corr with Precp (1957-2018; AMIP; Average of 17 Members & 10YR HP)
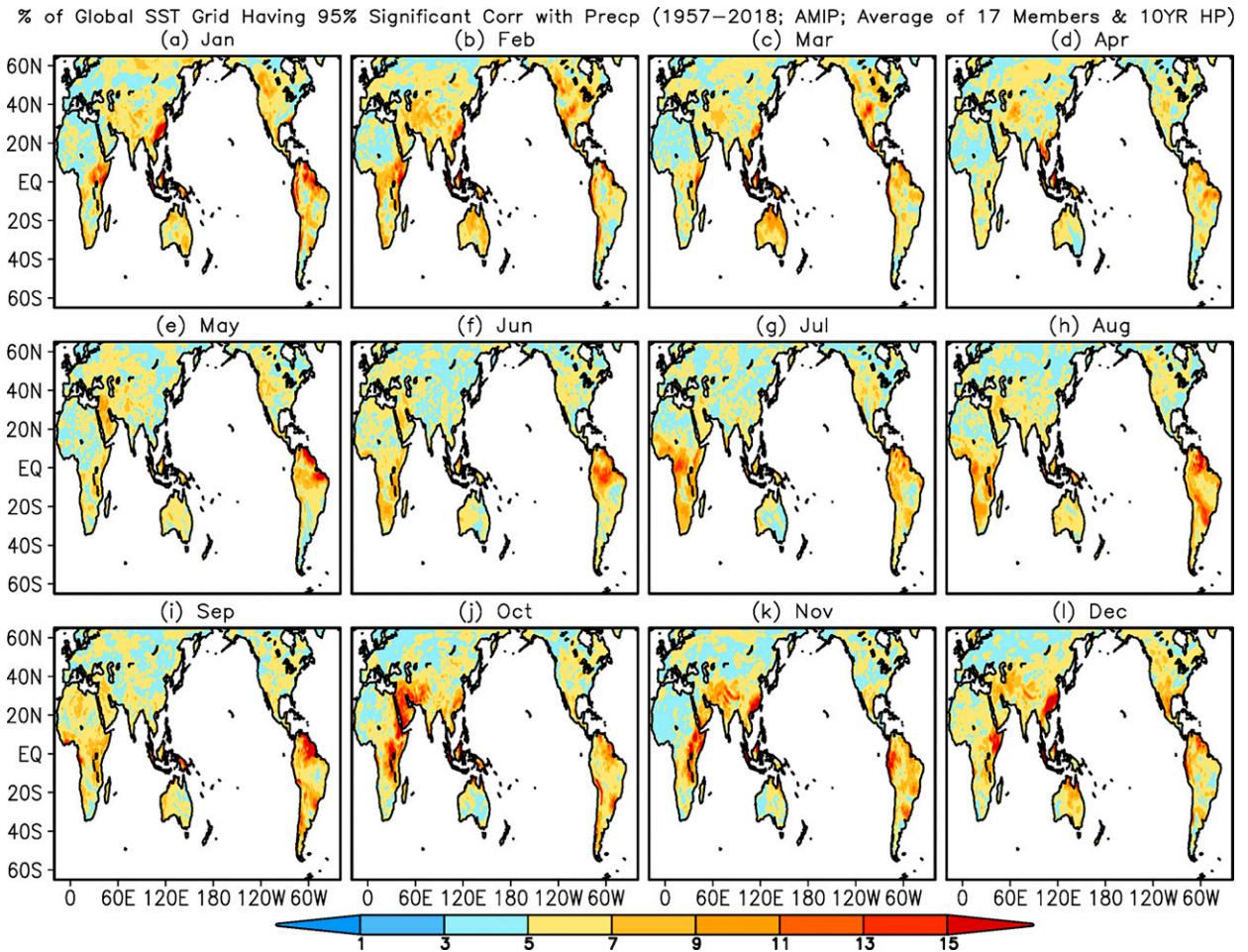

FIG. 7. As in Fig. 1, but for the average of BCs of 17 members of the AMIP simulations during January 1957–December 2018.

noise ratio (SNR; Fig. 9). Here, SNR refers to the ratio of the signal (the standard deviation of the ensemble mean of the 17 members) to the noise (the standard deviation of 17 individual members from the ensemble mean) in the AMIP simulations (Hu et al. 2019, 2020). To some extent, that confirms the fidelity of the BC metric in identifying the connection between two variables. Nevertheless, there is an appreciable difference in terms of the seasonality between Figs. 8 and 9. SNR has a maximum in the tropical SH in May to September, whereas BC has a maximum in the equatorial region in August to November. Also, compared with the latitudinal distribution in Figs. 2 and 8, the large SNR (Fig. 9) is more confined in the tropical regions, implying the unique feature of each method in examining the influence of boundary forcing on land precipitation variations. However, instead of identifying the connection between two variables, SNR-like approaches can be used to estimate predictability and average predictability time (Kumar et al. 2001; DelSole and Tippett 2009).

b. Ensemble mean of 17 members

Corresponding to the BC average for 17 individual members of the AMIP simulations shown in Figs. 7 and 8, Figs. 10 and 11

are the BC values calculated using the 17-member ensemble mean of the monthly mean precipitation and SST anomalies. The differences between the two methods of calculation are that the former approach (Figs. 7 and 8) is to calculate BC for each of 17 members first and then do the average of BCs, whereas the latter (Figs. 10 and 11) is to calculate the ensemble mean of the 17 members first and then compute the BCs of the ensemble mean. Compared with the 17-member averaged results (Figs. 7 and 8), the most profound change is the noticeable increase of the amplitudes, a consequence of eliminating the internal variability through the ensemble average.

5. Hemispheric averages and seasonality

The similarities and differences of BCs between the observations and the AMIP simulations are further examined through the Northern and Southern Hemisphere (NH and SH) averages (Fig. 12). First, the hemispheric averaged BC values in all months are larger than 5 in both the observations and the AMIP simulations, suggesting that SSTAs do have impacts on land precipitation anomaly as a whole in each month and each hemisphere. That implies predictability of land precipitation

Zonal Mean % of SST Grid Having 95% Significant Correlation with Land Precp (1957–2018; AMIP; Average of 17 Members & 10YR HP)
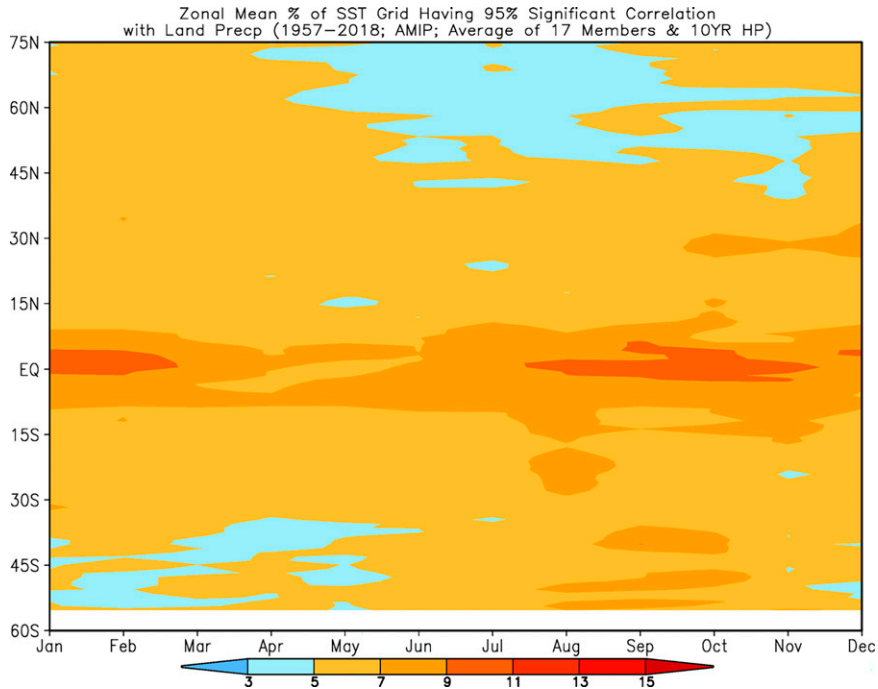
FIG. 8. As in Fig. 7, but for the zonal average.

variations to some extent. Second, the BC values are overall larger in the SH than the NH (the blue bars in Figs. 12a,b), suggesting that the integrated influence of SSTAs on land precipitation variations as a whole is larger in the SH than the NH in both the observations and AMIP simulations. Such hemispheric differences might occur because the SH has much smaller land area and a large portion of that land has connections with SST, while the NH as a whole aggregates regions that have and do

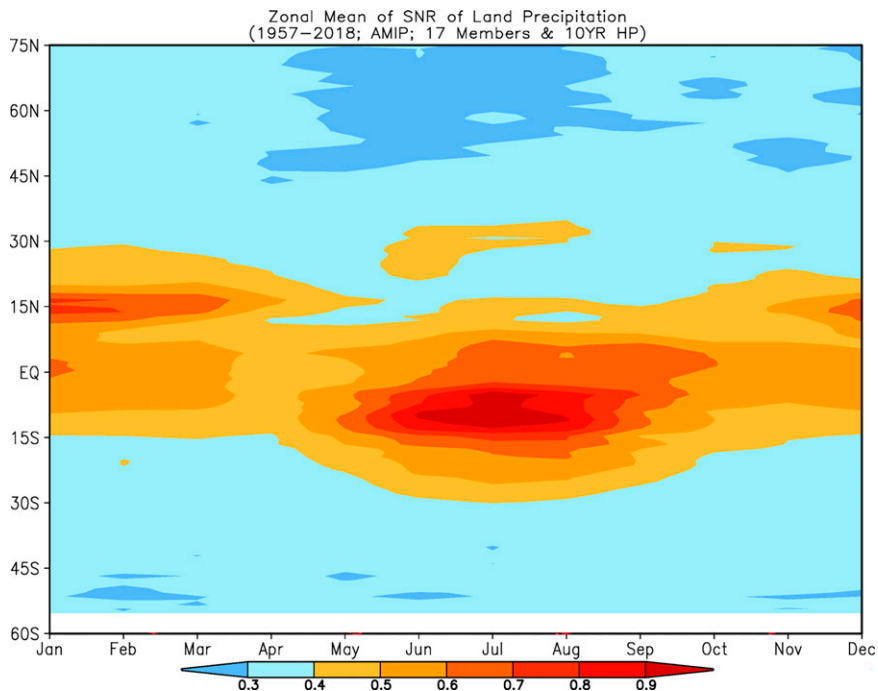Zonal Mean of SNR of Land Precipitation (1957–2018; AMIP; 17 Members & 10YR HP)

FIG. 9. Zonal mean of SNR of land precipitation in the AMIP simulations. Here, the signal refers to as the standard deviation of the ensemble mean of the 17 members, while the noise is defined as the standard deviation of 17 individual members from the ensemble mean.

% of Global SST Grid Having 95% Significant Corr with Precp (1957−2018; AMIP; Ensemble Mean & 10YR HP)
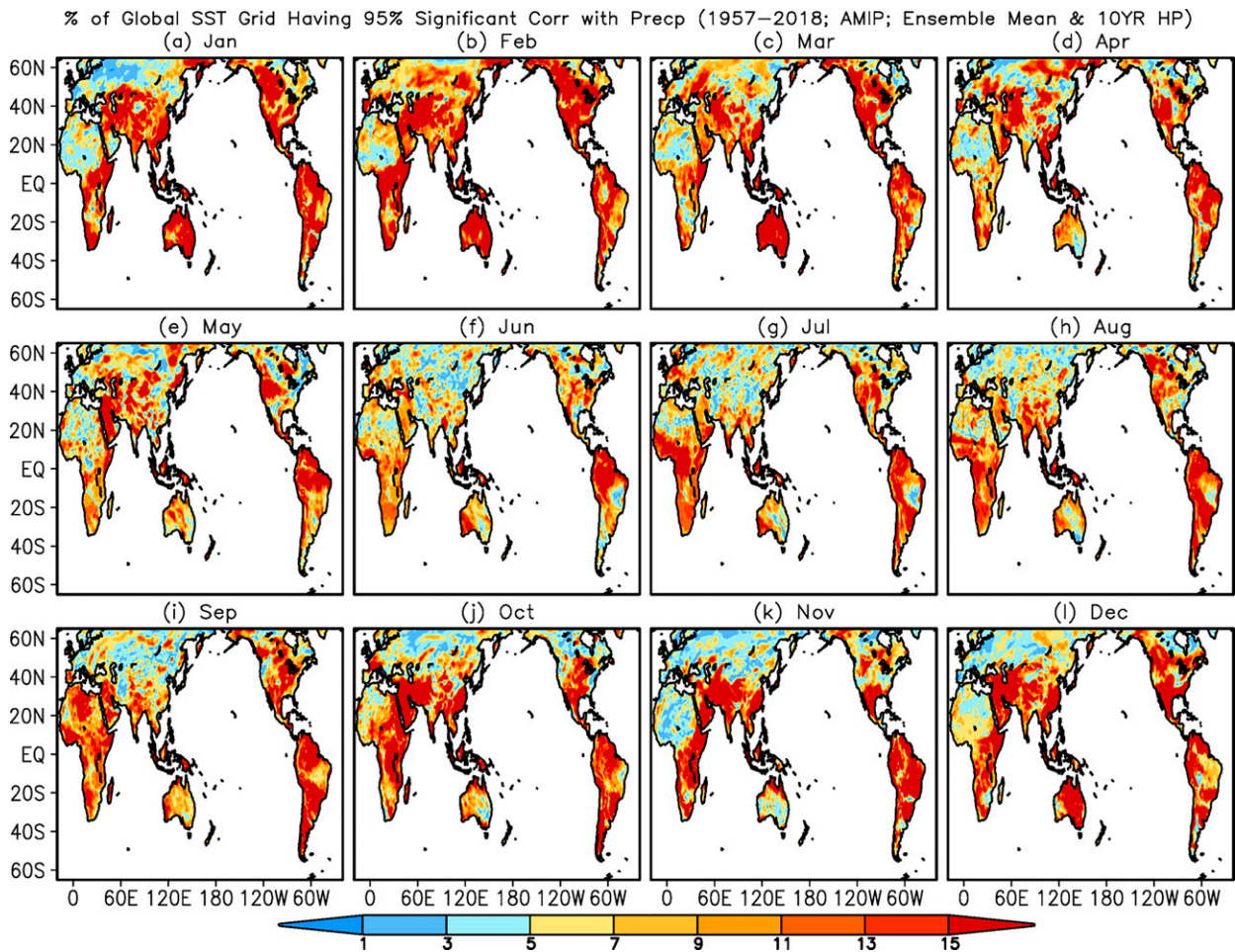
FIG. 10. As in Fig. 7, but for the ensemble mean of 17 members.

not have connections with SST. Third, the intensity of the impact shows clear seasonality that is more pronounced in the SH than the NH.

Compared with the observations (the blue bars in Fig. 12), the BC values are systematically underestimated in the 17-member average of the AMIP simulations in both hemispheres (particularly in the NH) (green bars in Fig. 12). Meanwhile, compared with the BC values themselves, the uncertainties (represented by one standard deviation among the 17 members' BCs, two horizontal green lines around the top of the green bars in Fig. 12) is relatively smaller, reflecting the robustness of the BC values of the 17 individual members in the AMIP simulations. This may be an indication that either the atmospheric internal variability in an individual run of the AMIP simulations is larger than the observations and/or the forced precipitation anomaly over land by the SSTAs is smaller (Li et al. 2022). Thus, in addition to sampling errors in the AMIP simulations, the internal variability driven by the atmospheric dynamical processes may also be an important factor leading to the differences between the observations and the BC average of the 17 members in the AMIP simulations (Figs. 1, 2, 7, and 8).

For the hemispheric average of monthly BC (Fig. 12), the ensemble mean values are much larger than those from both the observations and the 17-member averaged BCs of the AMIP simulations, indicating increases of the SNR. By suppressing the internal variability in the ensemble mean, the seasonality of the hemispheric averaged BC is also changed (Fig. 12; Table 1). In the ensemble mean of 17 members of the AMIP simulations of the NH (red bars in Fig. 12a), the maximum appears in February with BC = 13.6, and the minimum emerges in June with BC = 7.5. In the SH (red bars in Fig. 12b), the maximum appears in January with BC = 16.4, and the minimum emerges in June with BC = 10.5. Although the SNR of the integrated influence of the global SSTA on land precipitation anomaly in each hemisphere as a whole is enlarged in the ensemble mean, it still appears to be a challenge for both the individual members and their ensemble mean in the AMIP simulations to capture the observed seasonality of the integrated influence of global SSTA on land precipitation variations (Table 1). Since the observed SST is specified in the AMIP simulations, the seasonality biases must be due to the defects in the model. To examine what causes the seasonality biases, additional sensitivity experiments are needed that are beyond the scope of this work.
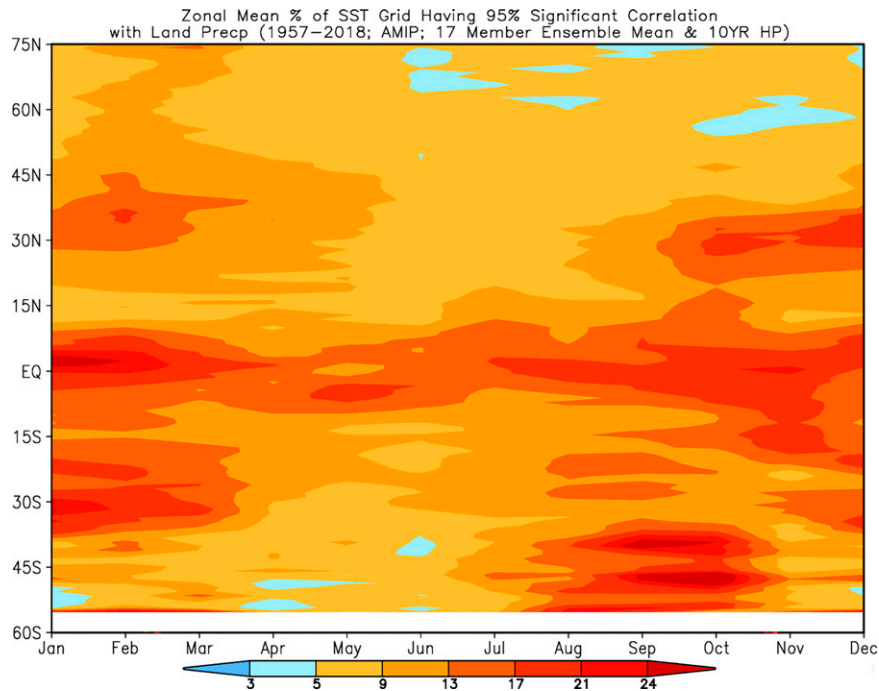
FIG. 11. As in Fig. 10, but for the zonal average.

Moreover, there are notable differences in the seasonality in both the BC amplitudes and the timings with maximum and minimum BCs between the observations and the 17-member average of the AMIP simulations (Table 1). In the NH observations (blue bars in Fig. 12a), the impact is the strongest in October with BC = 9.3, and the weakest in June with BC = 6.5. In other words, the strongest (weakest) impact of global SSTA on NH land precipitation variation in the observation occurs in October (June) with land precipitation variation significantly affected by the SSTA of about 9.3% (6.5%) ocean area at a 95% significance level. For the 17-member averages in NH (green bars in Fig. 12a), the BC value is the largest in February and December with BC = 6.3 and the smallest in June with BC = 5.3. In the SH observations (blue bars in Fig. 12b), the impact is the strongest in November with BC = 11.5, and the weakest in March with BC = 6.7. That suggests that the strongest (weakest) impact of global SSTA on SH land precipitation variation in the observation occurs in November (March) with land precipitation variation significantly affected by the SSTA of about 11.5% (6.7%) ocean area at a 95% significance level. For the 17-member averages in SH (green bars in Fig. 12b), the BC is the largest in August with BC = 7.4 and the smallest in April with BC = 5.9.

Overall, the results suggest that an individual run in the AMIP simulations underestimates the integrated influence of global SSTA on land precipitation anomalies, while the ensemble mean amplifies the integrated influence. In addition to the impact of biases in the AMIP simulations, including defects in the model and inaccuracy in the input (SST and greenhouse gas) forcings, on the results, the integrated influence of global SSTA on land precipitation anomalies and its seasonality, particularly the strongest SSTA influence season, is not accurately represented in the model. The difference between the observations and the ensemble mean of the AMIP simulations may represent the different features of the connection. In the ensemble mean of the AMIP simulations (Figs. 10 and 11), the precipitation variability reflects almost purely the response of the atmosphere (precipitation) anomaly to SSTA due to the suppression of the atmospheric internal dynamics–driven variability, while the connections in the observations represent a two-way interaction between the atmosphere and ocean that includes both the SSTA-forced response and the internal variability (Wu and Kirtman 2005; Wang et al. 2005; Zhu and Shukla 2013). It has been noted that the cancellation of the atmospheric dynamics-driven internal variability is effective with the increase of ensemble size from 1 to 10 (Hu et al. 2020). A consequence of the ensemble mean is to suppress the SST-unrelated internal variability, thus elevating the SNR (e.g., Kumar et al. 2001; Scaife and Smith 2018; Hu et al. 2020). Here, we should point out that the BC features in the tropics and extratropics may be quite different. In other words, the large-scale circulations connecting SST and tropical land precipitation may be distinct from the ones for extratropical land precipitation variations. Thus, the same hemispheric averaged BC value might not represent the same connection between SST and land precipitation.

6. Summary and discussion

Climate predictability at seasonal to interannual time scales is largely associated with SSTAs. How to quantitatively assess
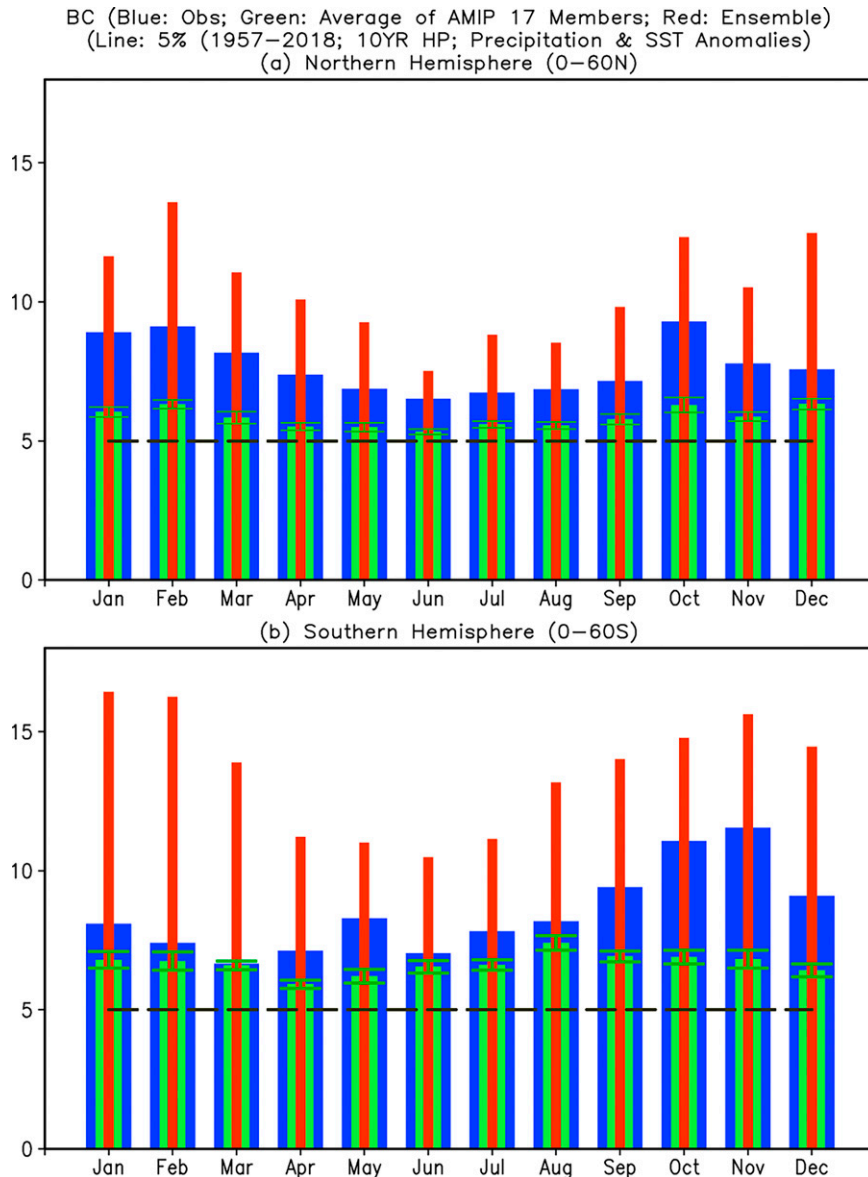
BC (Blue: Obs; Green: Average of AMIP 17 Members; Red: Ensemble)
(Line: 5% (1957−2018; 10YR HP; Precipitation & SST Anomalies)
(a) Northern Hemisphere (0−60N)

(b) Southern Hemisphere (0−60S)

FIG. 12. (a) Northern Hemispheric (0°–60°N) and (b) Southern Hemispheric (0°–60°S) averaged BCs of the observations (blue bars; Fig. 1), the mean of 17 members of the AMIP simulations (green bars; Fig. 7), and the ensemble mean of 17 members of the AMIP simulations (red bars; Fig. 10). The green horizontal error bars represent one standard deviation of the BC uncertainty of the 17 individual members. The horizontal dashed line is referred to as a 95% significance level of a *t* test.

the impact of SSTA on climate variability and predictability is an unresolved topic. Using the novel approach of the bulk connectivity (BC) metric, the integrated influences of the global SSTA as a whole on the precipitation anomalies over land are assessed using observations and AMIP simulations for 1957–2018. In the analyses, we identify the hotspots of the land precipitation variability affected by global SST and the seasonality. Such hotspot analysis provides a base for understanding the precipitation predictability. Moreover, through comparison with the results from the observation, the ability

of an individual member and the ensemble mean of the AMIP simulations to reproduce the influence and hotspots is evaluated.

In the observations, as expected, the values of BC decrease with the latitudinal increase, implying a decrease in the impact of SSTA on the predictability of land precipitation variations from low to high latitudes. There are land hotspots of the influence of SSTA in the global ocean as a whole on land precipitation variability, which vary with season. For instance, hotspots with large BC values occur in the

TABLE 1. Maximum and minimum BC values and the times.

	Observations	Average of 17 members	Ensemble mean of 17 members
NH maximum and time	9.3	6.3	13.6
	October	February and December	February
NH minimum and time	6.5	5.3	7.5
	June	June	June
SH maximum and time	11.5	7.4	16.4
	November	August	January
SH minimum and time	6.7	5.9	10.5
	March	April	June

Sahel region in September–March, in the Indochina Peninsula in April and May, and in the southwestern United States in December–March, suggesting the precipitation anomalies over these regions and months may be significantly affected by SSTA, in particular by the tropical Pacific SSTA associated with ENSO. Specifically, the large BC values between 0° and 15°N during January–April may be linked to the influence of ENSO on the precipitation anomalies in the Sahel region and the Indochina Peninsula, and large BC values in the tropics during July–December may reflect the collective impact of ENSO on the precipitation variations in the Sahel region, tropical Asia, the Maritime Continent, and tropical South America.

The influence of SSTA on land precipitation variations shows strong seasonality and varies with hemisphere. At the significance level of 95%, in the observations, the impact is the strongest in October with BC = 9.3, and the weakest in June with BC = 6.5 in NH, meaning that land precipitation variation is significantly affected by the SSTA of about 9.3% (6.5%) ocean area in October (June) in the NH. In the SH, the impact is the strongest in November with BC = 11.5, and the weakest in March with BC = 6.7, implying that land precipitation variation is significantly affected by the SSTA of about 11.5% (6.7%) ocean area in November (March) in the SH. The overall influence of SSTA on land precipitation variations is larger in the SH than the NH.

The spatial variations of BC and hotspots in the observations are partially reproduced in the AMIP simulations. An individual run in the AMIP simulations underestimates the integrated influence of global SSTA on land precipitation anomalies as a whole, while the ensemble mean amplifies the integrated influence. Nevertheless, although the signal-to-noise ratio increases noticeably in the ensemble mean of the AMIP simulations, it is still a challenge to reproduce the seasonality of the integrated influence of the global SSTA on land precipitation anomaly as a whole in either an individual member or multimember ensemble mean of the AMIP simulations, particularly the time of the strongest influence of the global SSTA on land precipitation anomalies. In fact, directly comparing BC from the ensemble mean with the observation is unfair. A more reasonable and idealized comparison is to use 17 observational/analyzed datasets from different sources (to mimic the ensemble simulations) to calculate the ensemble mean BC, and then compare it with the ensemble mean BC from the AMIP simulations.

In addition to the impact of biases in the AMIP simulations, the differences between the observations and the AMIP simulations may reflect different features for the generation of the atmospheric (precipitation) variability. In the observations, there is a two-way interaction between the atmosphere and ocean, while the atmospheric variability in the AMIP simulations includes both the atmospheric response to SSTA and internal variability driven by the internal dynamics. Such two-way interaction plays an important role in climate variability in some regions, such as the western North Pacific (Wu and Kirtman 2005; Wang et al. 2005; Zhu and Shukla 2013). It is unquestionable that the results from the AMIP simulations may be model dependent; thus, it is necessary to verify the results with the metric used in this work by analyzing AMIP simulations from other models or by examining fully coupled model results and to identify the impact of model biases on the results (Jha et al. 2014; Yuan et al. 2018; Wang et al. 2019; He et al. 2022).

It should be pointed out that in this work we focus on global SST; in other words, the calculation of BC aggregates the information over the entire ocean regardless of the basins. This might obscure some useful predictable signals. For example, if there is only a small fraction of the ocean that is beneficial for the prediction of certain regions' monthly precipitation, averaging over the global ocean will dilute the predictable signals. With that being said, the results based on BC will always identify the land precipitation associated with the largest-scale SST variability. Nevertheless, instead of global SST and global land precipitation, we can repeat the calculation with precipitation in a specified region and SST in a specified domain to examine if there are any significant connections between the precipitation in the region and SST in the domain. The BC metric used in this work can be treated as a survey-like examination to display the broad/bulk influence of global or tropical SST on global land precipitation. For a climate model, capturing such broad/bulk influence must be one of the preconditions for successful prediction of global land precipitation variation. Last, global warming trends and interdecadal variations may affect the influence of SST on land precipitation in the real world. For example, Jia et al. (2015) noted that the global warming signal and interdecadal variations are linked to a predictable pattern of seasonal forecasts of surface air temperature.

the NOAA CTB project (NA20OAR4590316). The scientific results and conclusions, as well as any view or opinions expressed herein, are those of the authors and do not necessarily reflect the views of NWS, NOAA, or the Department of Commerce.

Data availability statement: HadISST data are available online through https://climatedataguide.ucar.edu/climate-data/sst-data-hadisst-v11 and CRU data are from http://www.cru.uea.ac.uk/data, respectively. The AMIP simulations for this research are included in Hu et al. (2020), and Li et al. (2022).

REFERENCES

Alexander, L. V., P. Uotila, and N. Nicholls, 2009: Influence of sea surface temperature variability on global temperature and precipitation extremes. *J. Geophys. Res.*, **114**, D18116, https://doi.org/10.1029/2009JD012301.

Alexander, M. A., I. Blade, M. Newman, J. R. Lanzante, N.-C. Lau, and J. D. Scott, 2002: The atmospheric bridge: The influence of ENSO teleconnections on air–sea interaction over the global oceans. *J. Climate*, **15**, 2205–2231, https://doi.org/10.1175/1520-0442(2002)015<2205:TABTIO>2.0.CO;2.

Ashok, K., Z. Guan, and T. Yamagata, 2003: Influence of the Indian Ocean Dipole on Australian winter rainfall. *Geophys. Res. Lett.*, **30**, https://doi.org/10.1029/2003GL017926.

Bjerknes, J., 1969: Atmospheric teleconnections from the equatorial Pacific. *Mon. Wea. Rev.*, **97**, 163–172, https://doi.org/10.1175/1520-0493(1969)097<0163:ATFTEP>2.3.CO;2.

Cai, W., and Coauthors, 2019: Pantropical climate interactions. *Science*, **363**, eaav4236, https://doi.org/10.1126/science.aav4236.

Chen, M., P. Xie, J. E. Janowiak, and P. A. Arkin, 2002: Global land precipitation: A 50-yr monthly analysis based on gauge observations. *J. Hydrometeor.*, **3**, 249–266, https://doi.org/10.1175/1525-7541(2002)003<0249:GLPAYM>2.0.CO;2.

DelSole, T., and M. K. Tippett, 2009: Average predictability time. Part I: Theory. *J. Atmos. Sci.*, **66**, 1172–1187, https://doi.org/10.1175/2008JAS2868.1.

Harris, I., and Coauthors, 2020: Version 4 of the CRU TS monthly high-resolution gridded multivariate climate dataset. *Sci. Data*, **7**, 109, https://doi.org/10.1038/s41597-020-0453-3.

He, C., B. Wu, C. Li, A. Lin, D. Gu, B. Zheng, and T. Zhou, 2016: How much of the interannual variability of East Asian summer rainfall is forced by SST? *Climate Dyn.*, **47**, 555–565, https://doi.org/10.1007/s00382-015-2855-z.

——, Z. Cui, and C. Wang, 2022: Response of western North Pacific anomalous anticyclones in the summer of decaying El Niño to global warming: Diverse projections based on CMIP6 and CMIP5 models. *J. Climate*, **35**, 359–372, https://doi.org/10.1175/JCLI-D-21-0352.1.

He, S., J.-Y. Yu, S. Yang, and S.-W. Fang, 2020: ENSO's impacts on the tropical Indian and Atlantic Oceans via tropical atmospheric processes: Observations versus CMIP5 simulations. *Climate Dyn.*, **54**, 4627–4640, https://doi.org/10.1007/s00382-020-05247-w.

Hu, Z.-Z., A. Kumar, B. Huang, Y. Xue, W. Wang, and B. Jha, 2011: Persistent atmospheric and oceanic anomalies in the North Atlantic from summer 2009 to summer 2010. *J. Climate*, **24**, 5812–5830, https://doi.org/10.1175/2011JCLI4213.1.

——, ——, J. Zhu, P. Peng, and B. Huang, 2019: On the challenge for ENSO cycle prediction: An example from NCEP Climate Forecast System version 2. *J. Climate*, **32**, 183–194, https://doi.org/10.1175/JCLI-D-18-0285.1.

——, ——, B. Jha, and B. Huang, 2020: How much of monthly mean precipitation variability over global land is associated with SST anomalies? *Climate Dyn.*, **54**, 701–712, https://doi.org/10.1007/s00382-019-05023-5.

Jha, B., Z.-Z. Hu, and A. Kumar, 2014: SST and ENSO variability and change simulated in historical experiments of CMIP5 models. *Climate Dyn.*, **42**, 2113–2124, https://doi.org/10.1007/s00382-013-1803-z.

Jia, L., and Coauthors, 2015: Improved seasonal prediction of temperature and precipitation over land in a high-resolution GFDL climate model. *J. Climate*, **28**, 2044–2062, https://doi.org/10.1175/JCLI-D-14-00112.1.

Ju, J., and J. M. Slingo, 1995: The Asian summer monsoon and ENSO. *Quart. J. Roy. Meteor. Soc.*, **121**, 1133–1168, https://doi.org/10.1002/qj.49712152509.

Kayano, M. T., V. B. Rao, and A. D. Moura, 1988: Tropical circulations and the associated rainfall anomalies during two contrasting years. *J. Climate*, **8**, 477–488, https://doi.org/10.1002/joc.3370080504.

Kug, J.-S., and I.-S. Kang, 2006: Interactive feedback between ENSO and the Indian Ocean. *J. Climate*, **19**, 1784–1801, https://doi.org/10.1175/JCLI3660.1.

Kosaka, Y., J. S. Chowdary, S.-P. Xie, Y.-M. Min, and J.-Y. Lee, 2012: Limitations of seasonal predictability for summer climate over East Asia and the northwestern Pacific. *J. Climate*, **25**, 7574–7589, https://doi.org/10.1175/JCLI-D-12-00009.1.

Kumar, A., and M. P. Hoerling, 2003: The nature and causes for the delayed atmospheric response to El Niño. *J. Climate*, **16**, 1391–1403, https://doi.org/10.1175/1520-0442-16.9.1391.

——, A. G. Barnston, and M. P. Hoerling, 2001: Seasonal predictions, probabilistic verifications, and ensemble size. *J. Climate*, **14**, 1671–1676, https://doi.org/10.1175/1520-0442(2001)014<1671:SPPVAE>2.0.CO;2.

Lau, N. C., and M. J. Nath, 2003: Atmosphere–ocean variations in the Indo-Pacific sector during ENSO episodes. *J. Climate*, **16**, 3–20, https://doi.org/10.1175/1520-0442(2003)016<0003:AOVITI>2.0.CO;2.

Leathers, D. J., B. Yarnal, and M. A. Palecki, 1991: The Pacific/North American teleconnection pattern and United States climate. Part I: Regional temperature and precipitation associations. *J. Climate*, **4**, 517–528, https://doi.org/10.1175/1520-0442(1991)004<0517:TPATPA>2.0.CO;2.

Li, X., Z.-Z. Hu, P. Liang, and J. Zhu, 2019: Contrastive influence of ENSO and PNA on variability and predictability of North American winter precipitation. *J. Climate*, **32**, 6271–6284, https://doi.org/10.1175/JCLI-D-19-0033.1.

——, ——, B. Huang, and C. Stan, 2022: Bulk connectivity of global SST and land precipitation variations. *Climate Dyn.*, **58**, 195–209, https://doi.org/10.1007/s00382-021-05901-x.

Liang, P., Z.-Z. Hu, Y. Liu, X. Yuan, X. Li, and X. Jiang, 2019: Challenges in predicting and simulating summer rainfall in the eastern China. *Climate Dyn.*, **52**, 2217–2233, https://doi.org/10.1007/s00382-018-4256-6.

Mason, S. J., 2001: El Niño, climate change, and southern African climate. *Environmetrics*, **12**, 327–345, https://doi.org/10.1002/env.476.

National Research Council, 2010: *Assessment of Intraseasonal to Interannual Climate Prediction and Predictability*. The National Academies Press, 192 pp.

Nitta, T., 1987: Convective activities in the tropical western Pacific and their impact on the Northern Hemisphere summer

circulation. *J. Meteor. Soc. Japan*, **65**, 373–390, https://doi.org/10.2151/jmsj1965.65.3_373.

——, and Z.-Z. Hu, 1996: Summer climate variability in China and its association with 500 hPa height and tropical convection. *J. Meteor. Soc. Japan*, **74**, 425–445, https://doi.org/10.2151/jmsj1965.74.4_425.

O'Lenic, E. A., D. A. Unger, M. S. Halpert, and K. S. Pelman, 2008: Developments in operational long-range climate prediction at CPC. *Wea. Forecasting*, **23**, 496–515, https://doi.org/10.1175/2007WAF2007042.1.

Peng, P., A. Kumar, M. S. Halpert, and A. G. Barnston, 2012: An analysis of CPC's operational 0.5-month lead seasonal outlooks. *Wea. Forecasting*, **27**, 898–917, https://doi.org/10.1175/WAF-D-11-00143.1.

——, A. G. Barnston, and A. Kumar, 2013: A comparison of skill between two versions of the NCEP Climate Forecast System (CFS) and CPC's operational short-lead seasonal outlooks. *Wea. Forecasting*, **28**, 445–462, https://doi.org/10.1175/WAF-D-12-00057.1.

Rayner, N., P. Brohan, D. Parker, C. Folland, J. Kennedy, M. Vanicek, T. Ansell, and S. Tett, 2006: Improved analyses of changes and uncertainties in sea surface temperature measured in situ since the mid-nineteenth century: The HadSST2 data set. *J. Climate*, **19**, 446–469, https://doi.org/10.1175/JCLI3637.1.

Reynolds, R. W., N. A. Rayner, T. M. Smith, D. C. Stokes, and W. Wang, 2002: An improved in situ and satellite SST analysis for climate. *J. Climate*, **15**, 1609–1625, https://doi.org/10.1175/1520-0442(2002)015<1609:AIISAS>2.0.CO;2.

Ropelewski, C. F., and M. S. Halpert, 1987: Global and regional scale precipitation patterns associated with the El Niño/Southern Oscillation. *Mon. Wea. Rev.*, **115**, 1606–1626, https://doi.org/10.1175/1520-0493(1987)115<1606:GARSPP>2.0.CO;2.

——, and ——, 1996: Quantifying Southern Oscillation–precipitation relationships. *J. Climate*, **9**, 1043–1059, https://doi.org/10.1175/1520-0442(1996)009<1043:QSOPR>2.0.CO;2.

Saha, S., and Coauthors, 2014: The NCEP Climate Forecast System version 2. *J. Climate*, **27**, 2185–2208, https://doi.org/10.1175/JCLI-D-12-00823.1.

Scaife, A. A., and D. Smith, 2018: A signal-to-noise paradox in climate science. *npj Climate Atmos. Sci.*, **1**, 28, https://doi.org/10.1038/s41612-018-0038-4.

Stan, C., D. M. Straus, J. S. Frederiksen, H. Lin, E. D. Maloney, and C. Schumacher, 2017: Review of tropical–extratropical teleconnections on intraseasonal time scales. *Rev. Geophys.*, **55**, 902–937, https://doi.org/10.1002/2016RG000538.

Ting, M., and P. D. Sardeshmukh, 1993: Factors determining the extratropical response to equatorial diabatic heating anomalies. *J. Atmos. Sci.*, **50**, 907–918, https://doi.org/10.1175/1520-0469(1993)050<0907:FDTERT>2.0.CO;2.

Wallace, J. M., and D. S. Gutzler, 1981: Teleconnections in the geopotential height field during the Northern Hemisphere winter. *Mon. Wea. Rev.*, **109**, 784–812, https://doi.org/10.1175/1520-0493(1981)109<0784:TITGHF>2.0.CO;2.

Wang, B., R. Wu, and X. Fu, 2000: Pacific–East Asian teleconnection: How does ENSO affect East Asian climate? *J. Climate*, **13**, 1517–1536, https://doi.org/10.1175/1520-0442(2000)013<1517:PEATHD>2.0.CO;2.

——, Q. Ding, X. Fu, I.-S. Kang, K. Jin, J. Shukla, and F. Doblas-Reyes, 2005: Fundamental challenges in simulation and prediction of summer monsoon rainfall. *Geophys. Res. Lett.*, **32**, L15711, https://doi.org/10.1029/2005GL022734.

Wang, C., 2019: Three-ocean interactions and climate variability: A review and perspective. *Climate Dyn.*, **53**, 5119–5136, https://doi.org/10.1007/s00382-019-04930-x.

Wang, H., and R. Fu, 2000: Winter monthly mean atmospheric anomalies over the North Pacific and North America associated with El Niño SSTs. *J. Climate*, **13**, 3435–3447, https://doi.org/10.1175/1520-0442(2000)013<3435:WMMAAO>2.0.CO;2.

——, A. Kumar, and W. Wang, 2013: Characteristics of subsurface ocean response to ENSO assessed from simulations with the NCEP Climate Forecast System. *J. Climate*, **26**, 8065–8083, https://doi.org/10.1175/JCLI-D-12-00795.1.

Wang, Y., C. He, and T. Li, 2019: Decadal change in the relationship between East Asian spring circulation and ENSO: Is it modulated by Pacific Decadal Oscillation? *Int. J. Climatol.*, **39**, 172–187, https://doi.org/10.1002/joc.5793.

Wu, R., and B. P. Kirtman, 2005: Roles of Indian and Pacific Ocean air–sea coupling in tropical atmospheric variability. *Climate Dyn.*, **25**, 155–170, https://doi.org/10.1007/s00382-005-0003-x.

——, Z.-Z. Hu, and B. P. Kirtman, 2003: Evolution of ENSO-related rainfall anomalies in East Asia. *J. Climate*, **16**, 3742–3758, https://doi.org/10.1175/1520-0442(2003)016<3742:EOERAI>2.0.CO;2.

Xie, S.-P., K. M. Hu, J. Hafner, H. Tokinaga, Y. Du, G. Huang, and T. Sampe, 2009: Indian Ocean capacitor effect on Indo-western Pacific climate during the summer following El Niño. *J. Climate*, **22**, 730–747, https://doi.org/10.1175/2008JCLI2544.1.

——, Y. Kosaka, Y. Du, K. Hu, J. S. Chowdary, and G. Huang, 2016: Indo-western Pacific Ocean capacitor and coherent climate anomalies in post-ENSO summer: A review. *Adv. Atmos. Sci.*, **33**, 411–432, https://doi.org/10.1007/s00376-015-5192-6.

Yeh, S.-W., and Coauthors, 2018: ENSO atmospheric teleconnections and their response to greenhouse gas forcing. *Rev. Geophys.*, **56**, 185–206, https://doi.org/10.1002/2017RG000568.

Yuan, J., W. Li, R. E. Kopp, and Y. Deng, 2018: Response of subtropical stationary waves and hydrological extremes to climate warming in boreal summer. *J. Climate*, **31**, 10 165–10 180, https://doi.org/10.1175/JCLI-D-17-0401.1.

Yulaeva, E., and J. M. Wallace, 1994: The signature of ENSO in global temperature and precipitation fields derived from the Microwave Sounding Unit. *J. Climate*, **7**, 1719–1736, https://doi.org/10.1175/1520-0442(1994)007<1719:TSOEIG>2.0.CO;2.

Zhang, L., W. Han, and Z.-Z. Hu, 2021: Inter-basin and multi-time scale interactions in generating the 2019 extreme Indian Ocean dipole. *J. Climate*, 1–39, https://doi.org/10.1175/JCLI-D-20-0760.1.

Zhu, J., and J. Shukla, 2013: The role of air–sea coupling in seasonal prediction of Asia–Pacific summer monsoon rainfall. *J. Climate*, **26**, 5689–5697, https://doi.org/10.1175/JCLI-D-13-00190.1.